Uniform and Gaussian Ultraviolet Light Intensity Distribution on Droplet for Selective Area Deposition of Particles

Tianyi Li
Department of Mechanical Engineering,
University of Central Florida,
Orlando, FL 32816

Aravinda Kar
CREOL, The College of Optics and Photonics,
University of Central Florida,
Orlando, FL 32816

Ranganathan Kumar[1]
Department of Mechanical Engineering,
University of Central Florida,
Orlando, FL 32816
e-mail: ranganathan.kumar@ucf.edu

Particle transport through Marangoni convection inside a sessile droplet can be controlled by the ultraviolet (UV) light distribution on the surface. The photosensitive solution changes the surface tension gradient on the droplet surface and can induce clockwise and counterclockwise circulations depending on the incident light distribution. In this paper, the stream function in the sessile drop has been evaluated in toroidal coordinates by solving the biharmonic equation. Multiple primary clockwise and counterclockwise circulations are observed in the droplet under various concentric UV light profiles. The downward dividing streamlines are expected to deposit the particles on the substrate, thus matching the number of deposited rings on the substrate with the number of UV light rings. Moffatt eddies appear near the contact line or centerline of the droplet depending on the UV light profile and its distance from the contact line. [DOI: 10.1115/1.4047122]

Keywords: deposition, sessile drop, UV light

Introduction

Particle transport and depositing particles in a controlled manner have several important biological and industrial applications. Deposition of micro- and nanoparticles in straight airways has been studied by Hogberg et al. to understand the influence of the breathing pattern on the deposition of inhaled nonspherical micro- and nanoparticles [1]. It has also been reported that in duct flow, by enhancing the drag near the wall in a Newtonian fluid, nanoparticles agglomerate, and deposit on the wall [2]. Similarly, Lorentz force created by the flow induced by electric and magnetic fields is also found to enhance the particle deposition on the wall [3]. However, different methods to control and deposit nanoparticles at a desired location have been utilized for some time [4]. Through controlled evaporation in both horizontal and vertical directions, a monolayer of nanoparticles can be deposited due to coffee-ring effects [5,6]. External forces, such as shear stress and electrostatic force have also been applied for trapping the nanoparticles in desired position to assist with complex patterning as in

spin-coating, electrostatic deposition, and electrophoretic deposition [7–9]. With the assistance of water, some self-assembly nanoparticles can be directly assembled at the air–water interface as a monolayer and deposited on various substrates [10,11].

In recent research, by combining the micro-electrospray [12] and laser sintering, Eduardo et al. proposed a novel nanoparticle deposition method, nano-electrospray laser deposition, to deposit various nanoparticles on flexible or fixed substrates [13,14]. Another optical method of deposition, known as evaporative Optical Marangoni Assembly, applied UV light over a droplet of azoTAB solution to deposit the particles on the substrate experimentally [15–17]. AzoTAB is a kind of photosensitive surfactant having two isomers, tran-azoTAB and cis-azoTAB [18]. ultraviolet (UV)-conversion from trans to cis isomer of azoTAB increases the surface tension of the solution [19]. The surface tension induced flow, called Marangoni flow, has also been studied by evaluating the solutal Marangoni effect and the thermal Marangoni effect experimentally and analytically [20–23]. A theoretical framework in toroidal coordinates was developed to solve the Marangoni flow in sessile drop analytically with arbitrary contact angle [24], and a semi-analytical model has also been developed to find out the concentration of photosensitive particles in the hemispherical drop [25]. However, the Marangoni-induced particle deposition in a droplet under multiple UV light circles has not been studied.

In this study, the effect of concentric UV light with different beam widths and distributions on a sessile droplet of azoTAB solution has been studied by solving the stream function in the droplet analytically. The particles in the droplet following the stream function deposit on the substrate by the centrifugal force [26]. Relationships between the number and positions of the deposition rings and the UV light locations and distributions have also been addressed. Moffatt eddies are observed for certain light distributions, and are used to guide a preferable UV light pattern for desired depositions [27,28].

Methodology

In this study, the deposition position of the particles inside a hemispherical droplet of azoTAB solution under concentric UV light has been evaluated by solving the stream function of Marangoni flow inside a sessile droplet. Toroidal coordinates, shown in Fig. 1, described with toroid, spherical cap angle, and azimuthal angle (α, β, φ), are used to represent the geometry of a spherical cap droplet with radius R [24]. The driven force for the Marangoni flow is the surface tension gradient on the droplet surface, $\beta = \beta_c$, tuned by the UV light distribution and assumed to be a linear relationship with the UV light intensity [19]. The transition time between trans-azoTAB to cis-azoTAB can be as short as 0.1 s and thus is ignored [19]. As shown in Fig. 2, two types of concentric surface tension distribution, concentric rings of uniform distribution and concentric rings of Gaussian distribution due to the
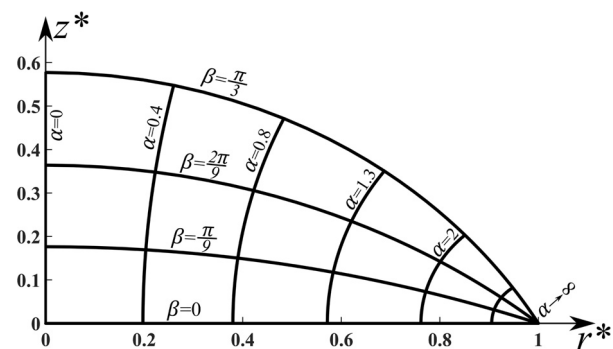
Fig. 1 Projection of toroidal coordinates system (α, β, ϕ) to a cylindrical coordinate (r^*, z^*, ϕ). $r^* = (r/R)$ represents the dimensionless radius and $z^* = (z/R)$ represents the dimensionless height.
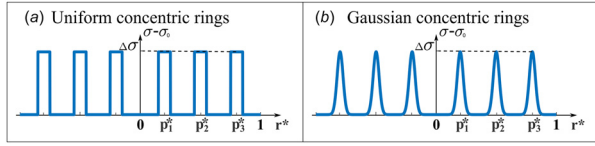
Fig. 2 Concentric surface tension distribution on droplet surface. $r^* = (r/R)$ represents the dimensionless axial distance away from the droplet center. p_1^*, p_2^*, and p_3^* denote the dimensionless average radii of concentric rings. (a) Surface tension profile for concentric rings of uniform distribution. (b) Surface tension profile for concentric rings of Gaussian distribution.

corresponding concentric UV light of the same shape, have been used as boundary conditions, in which the surface tension difference between the solution of cis-azoTAB and trans-azoTAB is defined as $\Delta\sigma$.

The characteristic velocity in the droplet due to surface tension gradient can be expressed as $V_0 = (\Delta\sigma/\mu)$, where μ is the dynamic viscosity of the azoTAB solution [24]. The expression of characteristic velocity due to evaporation is $V_e = J_0/\rho = \rho_g D(Y_s - Y_\infty)/\rho R$ [29], where ρ is the density of the azoTAB solution and ρ_g is the vapor density. $D = 22.5 \times 10^{-6}(T/273.15\,\text{K})^{1.8}\,\text{m}^2/\text{s}$ is the coefficient of binary diffusion of the vapor in the gas phase. Y_s and Y_∞ are the vapor mass fractions near the drop surface and far-field, respectively. R is the radius of the droplet. For droplets of 10 mM azoTAB solution with 3 mm radius under $22.5 \pm 1\,°\text{C}$ and relative humidity of $45 \pm 10\%$ which is used in Varanakkottu's experiment [15], $V_0 \sim 1\,\text{mm/s}$ and $V_e \sim 10^{-4}\,\text{mm/s}$. Since $V_e \ll V_0$, evaporation can be ignored for the conditions used in this simulation.

Defining the dimensionless stream function as $\psi^* = (\mu\psi)/(R^2\Delta\sigma)$, the biharmonic governing equation and boundary conditions for the stream function in toroidal coordinates can be written as

$$E^2(E^2\psi^*) = E^4\psi^* = 0 \tag{1}$$

$$\psi^*(0,\beta) = \psi^*(\alpha,0) = \psi^*(\alpha,\beta_c) = 0 \tag{2,3,4}$$

$$\frac{\partial\psi^*}{\partial\beta}\Big|_{\beta=0} = 0 \tag{5}$$

$$\frac{(\cosh\alpha + \cos\beta_c)}{\sinh\alpha}\left[(\cosh\alpha + \cos\beta_c)\frac{\partial\psi^{*2}}{\partial^2\beta}\Big|_{\beta_c} - 3\sin\beta_c \cdot \frac{\partial\psi^*}{\partial\beta}\Big|_{\beta_c}\right]$$
$$= \frac{1}{\Delta\sigma}\frac{\partial\sigma}{\partial\alpha}\Big|_{\beta_c} \tag{6}$$

$$\frac{\partial\psi^*}{\partial\beta}\Big|_{\alpha\to\infty} = \text{finite} \tag{7}$$

$$\frac{\partial\psi^*}{\partial\alpha}\Big|_{\alpha\to\infty} = \text{finite} \tag{8}$$

$$\frac{\partial\psi^*}{\partial\alpha}\Big|_{\alpha\to0} = \text{finite} \tag{9}$$

The final solution of the dimensionless stream function is found to be

$$\psi^*(\alpha,\beta) = (\cosh\alpha + \cos\beta)^{-\frac{3}{2}} \times \int_0^\infty K(\beta,\tau) \cdot C_{\frac{1}{2}+i\tau}^{-\frac{1}{2}}(\cosh\alpha)\,d\tau \tag{10}$$

where K is provided in the Appendix in Eqs. (A22)–(A29).

Results

The analytical results have been validated previously by comparing the predicted deposition location with the experimental particle deposition location [24]. In the experiment, a spherical cap droplet of radius 3 mm and contact angle 0.21π with 10 mM

azoTAB concentration has been illuminated under a circular uniformly distributed UV light whose inner and outer radii are 1.0 and 1.35 mm. The carboxylate polystyrene particles in the solution are deposited on the substrate forming a ring of inner and outer radii to be 1.0 and 1.27 mm corresponding to the nondimensional inner and outer radii to be 0.33 and 0.42. In the analytical solution, droplet of 10 mM azoTAB concentration with UV light of uniform distribution with dimensionless radius and ring width of 0.39 and 0.12, respectively, is considered. The droplet contact angle decreases from 0.21π to $\pi/9$. The analytical solutions for stream function are shown in Figs. 3(a) and 3(b) with the nondimensional inner and outer radii of the deposition patch of 0.33 and 0.37. The predicted deposition location by analytical solution matches the experimental deposition location very well in Fig. 3(c). This validation provides confidence that the current methodology will be able to predict the locations of concentric rings on the substrate for various light patterns incident on the sessile droplet.

The analytical results have been validated previously [24]. UV light of uniform distribution with dimensionless radius and ring width, $p^* = 0.39$ and $w^* = 0.12$, respectively, is illustrated in Fig. 3. The analytical solutions of stream function in sessile
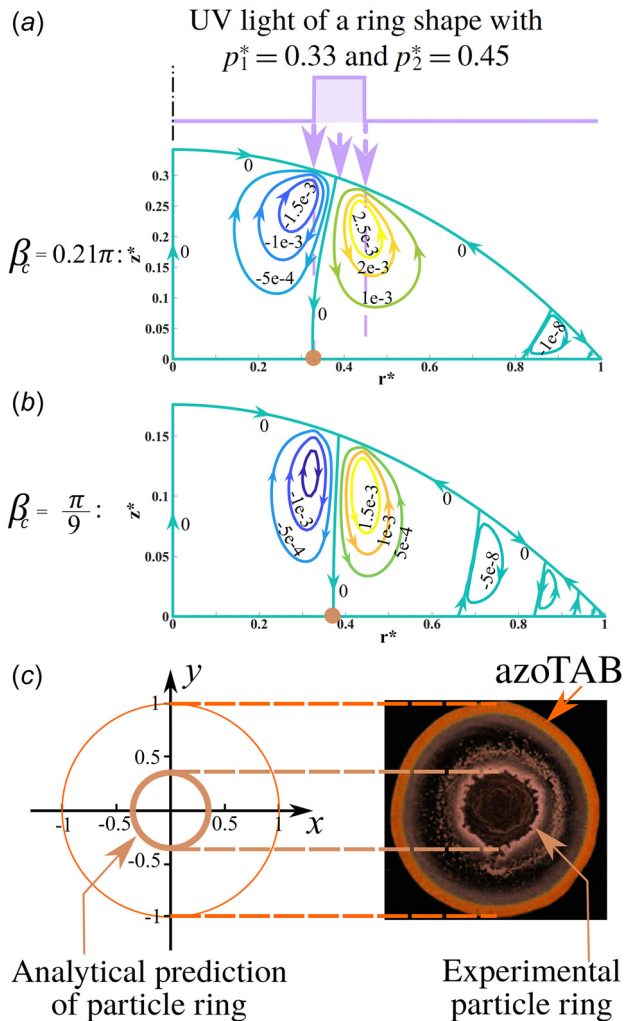
Fig. 3 Comparison of the particle deposition patterns in the analytical solutions and experiments for droplets under UV light ring of uniform distribution. Reprinted with permission from Li et al. [24]. Copyright 2019 by Cambridge University Press. ((a) and (b)) Stream functions and particle depositions by UV light ring of uniform distribution for droplet contact angle $\beta_c = 0.21\pi$ and $\beta_c = (\pi/9)$, respectively. (c) Comparison of the particle deposition between the analytical solution and in experiments by UV light ring of uniform distribution.
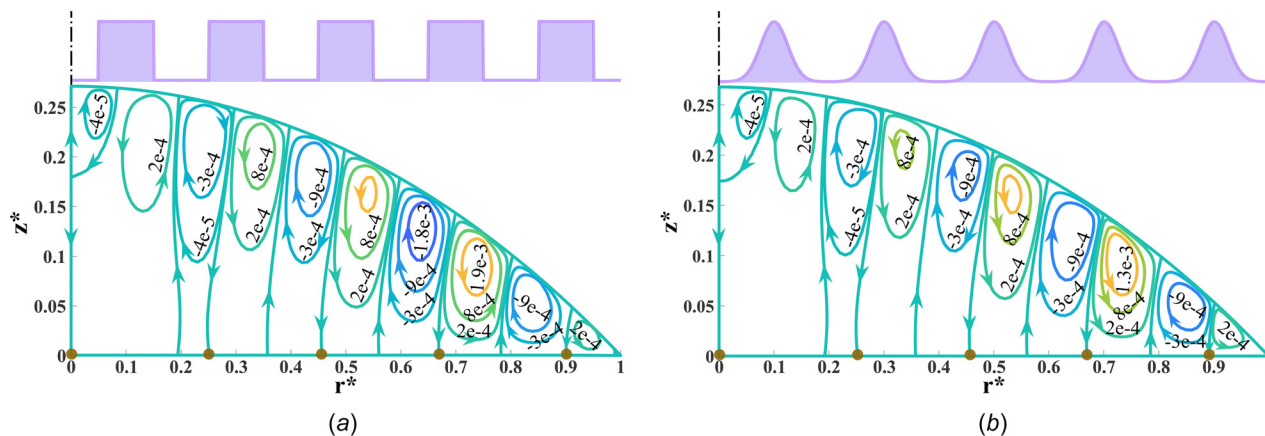
Fig. 4 Dimensionless stream function and particle deposition in droplet of $R = 1$ mm and $\beta_c = (\pi/6)$ with concentric surface tension distribution of $w^* = 0.1$ and $p^* = 0.1$, 0.3, 0.5, 0.7, and 0.9 for (a) uniform distribution and (b) Gaussian distribution
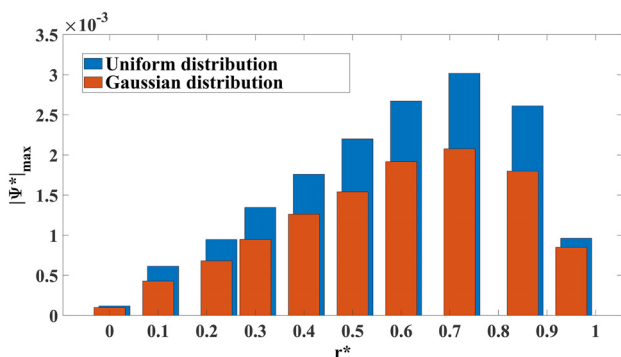
Fig. 5 Maximum absolute value of dimensionless stream function in each primary circulation cell in Fig. 4 for uniform and Gaussian distribution

droplets of contact angles 0.21π and $\pi/9$ are given in Figs. 3(a) and 3(b). Their expected deposition locations indicated by the intersection of the downward dividing streamline on the substrate are 0.33 and 0.37, respectively. In the experiments (Fig. 3(c)), the contact angle of the droplet changes from 0.21π to $\pi/9$ due to the evaporation during the whole deposition procedure and the inner and outer radii of the experimental deposited particle ring are 0.33 and 0.39, respectively, which are very close to the predicted locations in Figs. 3(a) and 3(b). Thus, the current methodology will be

able to predict the locations of concentric rings on the substrate for various light patterns incident on the sessile droplet.

Shown in Figs. 4(a) and 4(b) are flow patterns inside the sessile droplet for uniform and Gaussian distribution resulting in multiple counterclockwise and clockwise circulations. Multiple downward dividing streamlines are also observed in between the counter-rotating circulations which would deposit the nanoparticles on the substrate indicated by brown dots. Comparing the flow patterns due to uniform and Gaussian distribution with the same beam width, $w^* = 0.1$ and the same average radius, $p^* = 0.1$, 0.3, 0.5, 0.7, 0.9, the number, directions, sizes, and locations of the circulations in these two cases are visually the same, and thus their flow patterns inside the droplet appear to be very similar. However, the strength of each circulation by uniform distribution is higher than that due to Gaussian distribution at the same location as shown in Fig. 5.

Other than the larger primary circulations produced by the surface tension distribution, a small weak circulation appears near the contact line in Fig. 4(a), trapping particles inside and rotating without depositing on the substrate. This weak circulation is known as the Moffatt eddy whose strength is about 10^{-4} of other circulations. The interesting observation is that the Moffatt eddy does not appear for the Gaussian distribution (Fig. 4(b)) possibly because the gradient for the Gaussian distribution is smoother than that for the uniform light distribution.

When p^* is shifted slightly, the differences in the circulation patterns and deposition are similar. The Moffatt eddies appear in the uniform distribution and not in the Gaussian one. Based on these predictions and observations, possible relationships between
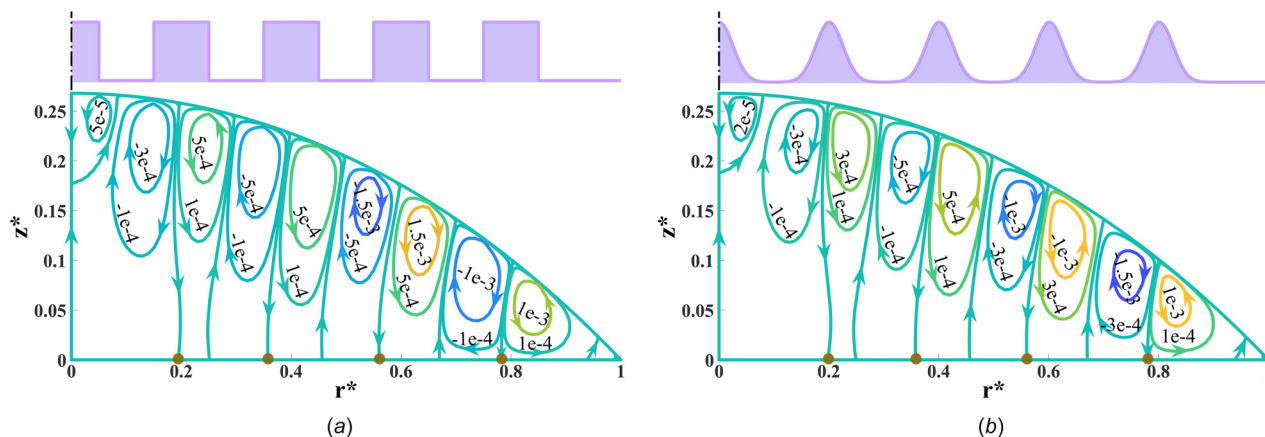
Fig. 6 Dimensionless stream function and particle deposition in droplet of $R = 1$ mm and $\beta_c = (\pi/6)$ with concentric surface tension distribution of $w^* = 0.1$ and $p^* = 0$, 0.2, 0.4, 0.6, and 0.8 for (a) uniform distribution and (b) Gaussian distribution
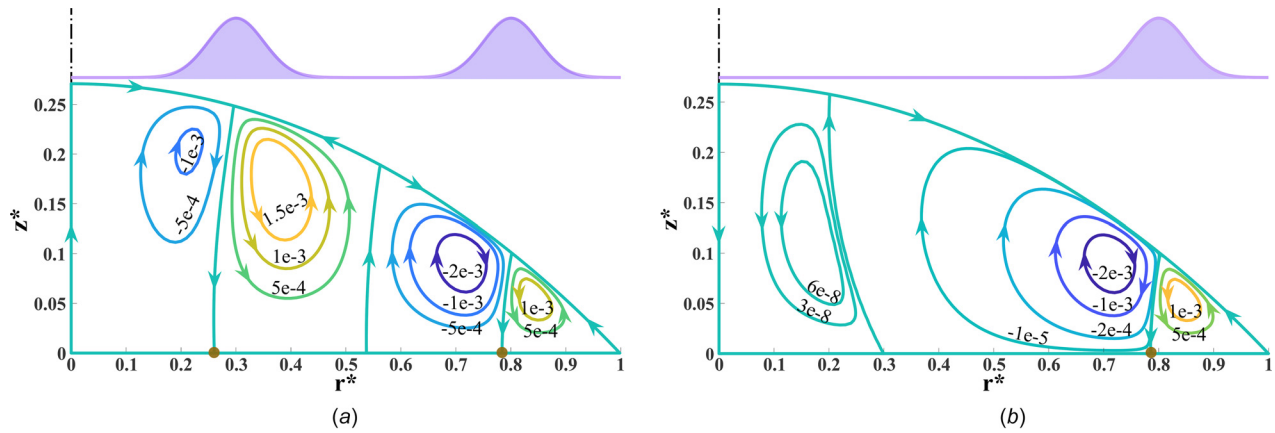
Fig. 7 Dimensionless stream function and particle deposition in droplet of $R = 1$ mm and $\beta_c = (\pi/6)$ with concentric rings of Gaussian distribution of $w^* = 0.2$ and (a) $p^* = 0.3$ and 0.8 (b) $p^* = 0.8$

the primary circulation and the Moffatt eddy patterns for a given UV light profile can be proposed. In both uniform and Gaussian distribution cases, each counterclockwise circulation or clockwise circulation appears around the peak of the light profile, respectively. The number of primary counterclockwise and clockwise circulations is equal to the number of light profile peaks. In addition, the downward dividing streamlines in between the counter-rotating circulations are located around the average radius of the concentric surface tension profile. This implies that the particles also deposit on the substrate near the average radius of the light profile. Once again, a stronger driving force occurs on the droplet due to the uniform light distribution, causing a stronger primary circulation.

It can be observed in Figs. 6(a) and 6(b) that Moffatt eddies appear in both uniform and Gaussian light profiles. This is contrary to what is observed in Fig. 4. Thus, it is not merely the sharp surface tension gradient of the uniform profile that contributes to the Moffatt eddies. It is also the location of the light profiles, i.e., p^*. In general, the Moffatt eddies are produced by the adjacent primary circulation near the contact line. When p^* of the last light beam is shifted from 0.9 (Fig. 4) to 0.8 (Fig. 6) or less, Moffatt eddies begin to appear. The key difference in the placement of the light beams over the droplet center is that particle deposition can be avoided at $r^* = 0$.

These observations can be further substantiated and exploited by placing a single beam close to the edge of the droplet, i.e., $p^* = 0.8$ and another at $p^* = 0.3$ as shown in Fig. 7. When both peaks are present (Fig. 7(a)), a counterclockwise circulation appears near the contact line, circulating the particles like a Moffatt eddy but contributing to the deposition. A series of clockwise and counterclockwise cells appear, depositing the particles at $r^* = 0.25$ and $r^* = 0.8$. When the light beam closer to the droplet center is removed, the cell that previously allowed the deposition of particles at $r^* = 0.8$ becomes very large and continues to deposit at $r^* = 0.8$ (Fig. 7(b)). However, since the light beam at $p^* = 0.3$ is removed now, there is no other deposition location on the substrate. A weaker counterclockwise cell appears near the droplet center, without depositing particles at the center of the droplet. It is possible that most of the particles are deposited at $r^* = 0.8$. Thus, when the Moffatt eddies are created either near the contact line or centerline adjacent to the primary circulation, those Moffatt eddies occupy only a small region of the droplet and circulate the particles without depositing them on the substrate.

Conclusion

The effect of concentric uniform and Gaussian UV light intensity distribution with different beam widths on a sessile droplet of azoTAB solution has been analytically studied. Stream functions

have been obtained for both types of light distribution inducing a surface tension gradient which drives the Marangoni convection in the droplet. The surface tension profile creates a primary clockwise or counterclockwise circulation, and the downward dividing streamline allows the particles to deposit on the substrate at desired locations. Thus, it is possible to determine and control the locations of the deposition ring patterns on the substrate by a priori by manipulating the location of the light beam over the droplet.

Several observations were made in this study. By suitably positioning the beam peak away from the droplet center and edge, it is possible to create Moffatt eddies that carry the particles while weakly circulating, but do not deposit them on the substrate. The Moffatt eddies can appear both at the center and the edge. Such an orientation of the beam peaks would be preferred if concentric deposition patterns are not desirable either at the center or at the edge. For both types of light distributions, the average radii of the concentric light beams should match the desired deposition positions since the particles deposit on the substrate where the UV light is illuminated. Thus, it is possible to infer that any shape of deposition is possible if a similar light beam illuminates the droplet from the top.

Funding Data

Nomenclature

D = coefficient of binary diffusion of the vapor in the gas phase
J_0 = water mass flux at the droplet surface
p^* = average radius of concentric ring
r = distance away from droplet centerline
R = droplet radius on the substrate
r^* = dimensionless r (r/R)
V_e = characteristic velocity by evaporation
V_0 = characteristic velocity by surface tension gradient
w^* = dimensionless beam width
Y_s = vapor mass fraction near the droplet surface
Y_∞ = vapor mass fraction far away from the droplet surface
α = toroids in toroidal coordinate
β = spherical cap angle in toroidal coordinate
β_c = contact angle of the droplet
$\Delta\sigma$ = surface tension difference
μ = dynamic viscosity
ρ = density of the azoTAB solution
ρ_g = density of the vapor

σ = surface tension
ϕ = azimuthal angle in toroidal coordinate
ψ = stream function
ψ^* = dimensionless stream function

Appendix

Derivations for the boundary conditions and solution of the dimensionless stream function $\psi^*(\alpha, \beta) < /b >$.

The governing equation for dimensionless stream function of Stokes flow in toroidal coordinates is expressed as $E^4 \psi^* = E^2(E^2 \psi^*) = 0$ [24]

$$E^2 = \sinh\alpha(\cosh\alpha + \cos\beta)\left[\frac{\partial}{\partial\alpha}\left(\frac{\cosh\alpha + \cos\beta}{\sinh\alpha}\frac{\partial}{\partial\alpha}\right) + \frac{\partial}{\partial\beta}\left(\frac{\cosh\alpha + \cos\beta}{\sinh\alpha}\frac{\partial}{\partial\beta}\right)\right] \quad (A1)$$

The expressions for the dimensionless velocities in toroidal coordinate in terms of dimensionless stream function are

$$V_\alpha^* = \frac{(\cosh\alpha + \cos\beta)^2}{\sinh\alpha}\frac{\partial\psi}{\partial\beta} \quad (A2)$$

$$V_\beta^* = -\frac{(\cosh\alpha + \cos\beta)^2}{\sinh\alpha}\frac{\partial\psi}{\partial\alpha} \quad (A3)$$

The boundary conditions for the dimensionless stream function are converted from the dimensionless velocity boundary conditions. Normal to the rotation axis of symmetry, the velocity is zero

$$V_\alpha^*(0, \beta) = 0 \rightarrow \frac{\partial\psi^*}{\partial\beta}|_{\alpha=0} = 0 \rightarrow \psi^*(0, \beta) = C_1 \quad (A4)$$

The no-slip boundary condition is applied to the substrate

$$V_\alpha^*(\alpha, 0) = 0 \rightarrow \frac{\partial\psi^*}{\partial\beta}|_{\beta=0} = 0 \quad (A5)$$

$$V_\beta^*(0, \beta) = 0 \rightarrow \frac{\partial\psi^*}{\partial\alpha}|_{\beta=0} = 0 \rightarrow \psi^*(\alpha, 0) = C_2 \quad (A6)$$

On the droplet surface, where $\beta = \beta_c$, the normal velocity is zero

$$V_\beta^*(0, \beta_c) = 0 \rightarrow \frac{\partial\psi^*}{\partial\alpha}|_{\beta=\beta_c} = 0 \rightarrow \psi^*(\alpha, \beta_c) = C_3 \quad (A7)$$

C_1, C_2, and C_3 are set to be 0

$$\psi^*(0, \beta) = \psi^*(\alpha, 0) = \psi^*(\alpha, \beta_c) = 0 \quad (A8,A9,A10)$$

Tangential to the droplet surface, the shear stress and surface tension are balanced

$$\tau_{\alpha\beta} = \mu\left\{\frac{\partial}{\partial\alpha}\left[(\cosh\alpha + \cos\beta)\frac{V_\beta}{R}\right] + \frac{\partial}{\partial\beta}\left[(\cosh\alpha + \cos\beta)\frac{V_\alpha}{R}\right]\right\}|_{\beta=\beta_c} \quad (A11)$$

Since $V_\beta^*(0, \beta_c) = 0$, Eq. (A11) can be further simplified as

$$\tau_{\alpha\beta} = \mu\frac{(\cosh\alpha + \cos\beta_c)^2}{R^3\sinh\alpha}\left[(\cosh\alpha + \cos\beta_c)\frac{\partial^2\psi}{\partial\beta^2} - 3\sin\beta_c\frac{\partial\psi}{\partial\beta}\right]|_{\beta=\beta_c} \quad (A12)$$

The shear stress matches the surface tension gradient gives

$$\tau_{\alpha\beta} = \frac{\cosh\alpha + \cos\beta_c}{R}\frac{\partial\sigma}{\partial\alpha}|_{\beta_c} \quad (A13)$$

Insert Eq. (A13) to Eq. (A12) and nondimensionalize it to get

$$\frac{(\cosh\alpha + \cos\beta_c)}{\sinh\alpha}\left[(\cosh\alpha + \cos\beta_c)\frac{\partial^2\psi^*}{\partial\beta^2} - 3\sin\beta_c\frac{\partial\psi^*}{\partial\beta}\right]\bigg|_{\beta=\beta_c}$$
$$= \frac{1}{\Delta\sigma}\frac{\partial\sigma}{\partial\alpha}\bigg|_{\beta_c} \quad (A14)$$

The other three boundary conditions are the nonsingular boundary conditions at the axis of symmetry as well as at the contact line

$$V_\beta^*(0, \beta) = \text{finite} \rightarrow \frac{(\cosh\alpha + \cos\beta)^2}{\sinh\alpha}\frac{\partial\psi^*}{\partial\alpha}|_{\alpha=0} = \text{finite} \quad (A15)$$

$$V_\beta^*(\alpha \rightarrow \infty, \beta) = \text{finite} \rightarrow \frac{(\cosh\alpha + \cos\beta)^2}{\sinh\alpha}\frac{\partial\psi^*}{\partial\alpha}|_{\alpha\rightarrow\infty} = \text{finite} \quad (A16)$$

$$V_\alpha^*(\alpha \rightarrow \infty, \beta) = \text{finite} \rightarrow \frac{(\cosh\alpha + \cos\beta)^2}{\sinh\alpha}\frac{\partial\psi^*}{\partial\beta}|_{\alpha\rightarrow\infty} = \text{finite} \quad (A17)$$

The general solution of the biharmonic governing equation is

$$\psi^*(\alpha, \beta) = (\cosh\alpha + \cos\beta)^{-\frac{3}{2}} \times \int_0^\infty \left[A(\tau)C_{\frac{1}{2}+i\tau}^{-\frac{1}{2}}(\cosh\alpha) + B(\tau)C_{\frac{1}{2}+i\tau}^{*-\frac{1}{2}}(\cosh\alpha)\right] \times \left\{\sinh\tau\beta[C(\tau)\sin\beta + D(\tau)\cos\beta] + \cosh\tau\beta[E(\tau)\sin\beta + F(\tau)\cos\beta]\right\} d\tau \quad (A18)$$

where $C_{\frac{1}{2}+i\tau}^{-\frac{1}{2}}(\cosh\alpha)$ and $C_{\frac{1}{2}+i\tau}^{*-\frac{1}{2}}(\cosh\alpha)$ are the first and second kind Gegenbauer functions of degree $\frac{1}{2}$ and order $\frac{1}{2} + i\tau$ with i to be the imaginary unit. Their relationships with the first and second kind Legendre polynomials, $P_{\frac{1}{2}+i\tau}(\cosh\alpha)$ and $Q_{\frac{1}{2}+i\tau}(\cosh\alpha)$ can be expressed as [30]

$$C_{\frac{1}{2}+i\tau}^{-\frac{1}{2}}(\cosh\alpha) = \frac{1}{2i\tau}\left[P_{-\frac{3}{2}+i\tau}(\cosh\alpha) - P_{\frac{1}{2}+i\tau}(\cosh\alpha)\right] \quad (A19)$$

$$C_{\frac{1}{2}+i\tau}^{*-\frac{1}{2}}(\cosh\alpha) = \frac{1}{2i\tau}\left[Q_{-\frac{3}{2}+i\tau}(\cosh\alpha) - Q_{\frac{1}{2}+i\tau}(\cosh\alpha)\right] \quad (A20)$$

Applying boundary condition Eq. (A8) to Eq. (A18), $B(\tau) = 0$ for $C_{\frac{1}{2}+i\tau}^{*-\frac{1}{2}}(\cosh\alpha)|_{\alpha=0} \neq 0$. Boundary condition Eq. (A9) gives $F(\tau) = 0$ and Eq. (A5) gives $E(\tau) = -\tau D(\tau)$. The nondimensional stream function can be converted to

$$\psi^*(\alpha, \beta) = (\cosh\alpha + \cos\beta)^{-\frac{3}{2}} \times \int_0^\infty K(\beta, \tau) \cdot C_{\frac{1}{2}+i\tau}^{-\frac{1}{2}}(\cosh\alpha) d\tau \quad (A21)$$

with

$$K(\beta, \tau) = k_1(\tau)\sin\beta\sinh(\tau\beta) + k_2(\tau)[\cos\beta\sinh(\tau\beta) - \tau\sin\beta\cosh(\tau\beta)] \quad (A22)$$

Insert Eq. (A10) to Eq. (A21) to find out the relationship between $k_1(\tau)$ and $k_2(\tau)$ as

$$k_2(\tau) = -k_1(\tau)\frac{\sin\beta_c \cdot \sinh(\tau\beta_c)}{\cos\beta_c \cdot \sinh(\tau\beta_c) - \tau\sin\beta_c \cdot \cosh(\tau\beta_c)} \quad (A23)$$

And apply Eq. (A14) with Eq. (A23) to Eq. (A21) to solve $k_1(\tau)$ as

$$k_1(\tau) = \frac{N_1 \cdot N_2}{M_1 + M_2 \cdot M_3} \quad (A24)$$

in which

$$N_1 = \tau\left(\tau^2 + \frac{1}{4}\right)\tanh(\pi\tau) \tag{A25}$$

$$N_2 = \int_0^\infty (\cosh\alpha + \cos\beta_c)^{-\frac{1}{2}} \cdot \frac{\partial\sigma}{\Delta\sigma\partial\alpha}|_{\beta_c} \cdot C_{\frac{1}{2}+i\tau}^{-\frac{1}{2}}(\cosh\alpha)d\alpha \tag{A26}$$

$$M_1 = 2\tau \cdot \cos\beta_c\cosh(\tau\beta_c) + (\tau^2 - 1) \cdot \sin\beta_c\sinh(\tau\beta_c) \tag{A27}$$

$$M_2 = (\tau^2 + 1)\cos\beta_c\sinh(\tau\beta_c) + (\tau + \tau^3)\sin\beta_c\cosh(\tau\beta_c) \tag{A28}$$

$$M_3 = \frac{\sin\beta_c \cdot \sinh(\tau\beta_c)}{\cos\beta_c \cdot \sinh(\tau\beta_c) - \tau\sin\beta_c \cdot \cosh(\tau\beta)} \tag{A29}$$

The rest of the boundary conditions, Eqs. (A15)–(A17), are non-singular boundary conditions and are satisfied automatically.

References

[1] Högberg, S. M., Åkerstedt, H. O., Holmstedt, E., Staffan Lundström, T., and Sandström, T., 2012, "Time-Dependent Deposition of Micro-and Nanofibers in Straight Model Airways," ASME J. Fluids Eng., **134**(5), p. 051208.

[2] Michaelides, E. E., 2016, "Wall Effects on the Brownian Movement, Thermophoresis, and Deposition of Nanoparticles in Liquids," ASME J. Fluids Eng., **138**(5), p. 051303.

[3] Liu, R., Vanka, S. P., and Thomas, B. G., 2014, "Particle Transport and Deposition in a Turbulent Square Duct Flow With an Imposed Magnetic Field," ASME J. Fluids Eng., **136**(12), p. 121201.

[4] Vogel, N., Retsch, M., Fustin, C. A., Del Campo, A., and Jonas, U., 2015, "Advances in Colloidal Assembly: The Design of Structure and Hierarchy in Two and Three Dimensions," Chem. Rev., **115**(13), pp. 6265–6311.

[5] Haes, A. J., and Van Duyne, R. P., 2002, "A Nanoscale Optical Biosensor: Sensitivity and Selectivity of an Approach Based on the Localized Surface Plasmon Resonance Spectroscopy of Triangular Silver Nanoparticles," J. Am. Chem. Soc., **124**(35), pp. 10596–10604.

[6] Armstrong, E., Khunsin, W., Osiak, M., Blömker, M., Torres, C. M. S., and O'Dwyer, C., 2014, "Ordered 2D Colloidal Photonic Crystals on Gold Substrates by Surfactant-Assisted Fast-Rate Dip Coating," Small, **10**(10), pp. 1895–1901.

[7] Mihi, A., Ocaña, M., and Míguez, H., 2006, "Oriented Colloidal-Crystal Thin Films by Spin-Coating Microspheres Dispersed in Volatile Media," Adv. Mater., **18**(17), pp. 2244–2249.

[8] Zhang, X., Zhang, J., Zhu, D., Li, X., Zhang, X., Wang, T., and Yang, B., 2010, "A Universal Approach to Fabricate Ordered Colloidal Crystals Arrays Based on Electrostatic Self-Assembly," Langmuir, **26**(23), pp. 17936–17942.

[9] Dziomkina, N. V., Hempenius, M. A., and Vancso, G. J., 2005, "Symmetry Control of Polymer Colloidal Monolayers and Crystals by Electrophoretic Deposition on Patterned Surfaces," Adv. Mater., **17**(2), pp. 237–240.

[10] Sirotkin, E., Apweiler, J. D., and Ogrin, F. Y., 2010, "Macroscopic Ordering of Polystyrene Carboxylate-Modified Nanospheres Self-Assembled at the Water-Air Interface," Langmuir, **26**(13), pp. 10677–10683.

[11] Meng, X., and Qiu, D., 2014, "Gas-Flow-Induced Reorientation to Centimeter-Sized Two-Dimensional Colloidal Single Crystal of Polystyrene Particle," Langmuir, **30**(11), pp. 3019–3023.

[12] Castillo-Orozco, E., Kar, A., and Kumar, R., 2017, "Electrospray Mode Transition of Microdroplets With Semiconductor Nanoparticle Suspension," Sci. Rep., **7**(1), pp. 1–10.

[13] Castillo-Orozco, E., Kumar, R., and Kar, A., 2019, "Laser Electrospray Printing of Nanoparticles on Flexible and Rigid Substrates," J. Laser Appl., **31**(2), p. 022015.

[14] Castillo-Orozco, E., Kumar, R., and Kar, A., 2019, "Laser-Induced Subwavelength Structures by Microdroplet Superlens," Opt. Express, **27**(6), pp. 8130–8142.

[15] Varanakkottu, S. N., Anyfantakis, M., Morel, M., Rudiuk, S., and Baigl, D., 2016, "Light-Directed Particle Patterning by Evaporative Optical Marangoni Assembly," Nano Lett., **16**(1), pp. 644–650.

[16] Anyfantakis, M., Varanakkottu, S. N., Rudiuk, S., Morel, M., and Baigl, D., 2017, "Evaporative Optical Marangoni Assembly: Tailoring the Three-Dimensional Morphology of Individual Deposits of Nanoparticles from Sessile Drops," ACS Appl. Mater. Interfaces, **9**(42), pp. 37435–37445.

[17] Anyfantakis, M., and Baigl, D., 2014, "Dynamic Photocontrol of the Coffee-Ring Effect With Optically Tunable Particle Stickiness," Angew. Chem., Int. Ed., **53**(51), pp. 14077–14081.

[18] Brown, P., Butts, C. P., and Eastoe, J., 2013, "Stimuli-Responsive Surfactants," Soft Matter, **9**(8), pp. 2365–2374.

[19] Chevallier, E., Mamane, A., Stone, H. A., Tribet, C., Lequeux, F., and Monteux, C., 2011, "Pumping-Out Photo-Surfactants From an Air-Water Interface Using Light," Soft Matter., **7**(17), p. 7866.

[20] Marin, A., Liepelt, R., Rossi, M., and Kähler, C. J., 2016, "Surfactant-Driven Flow Transitions in Evaporating Droplets," Soft Matter., **12**(5), pp. 1593–1600.

[21] Diddens, C., Tan, H., Lv, P., Versluis, M., Kuerten, J. G. M., Zhang, X., and Lohse, D., 2017, "Evaporating Pure, Binary and Ternary Droplets: Thermal Effects and Axial Symmetry Breaking," J. Fluid Mech., **823**, pp. 470–497.

[22] Ristenpart, W. D., Kim, P. G., Domingues, C., Wan, J., and Stone, H. A., 2007, "Influence of Substrate Conductivity on Circulation Reversal in Evaporating Drops," Phys. Rev. Lett., **99**(23), p. 234502.

[23] Tam, D., von Arnim, V., McKinley, G. H., and Hosoi, A. E., 2009, "Marangoni Convection in Droplets on Superhydrophobic Surfaces," J. Fluid Mech., **624** pp. 101–123.

[24] Li, T., Kar, A., and Kumar, R., 2019, "Marangoni Circulation by UV Light Modulation on Sessile Drop for Particle Agglomeration," J. Fluid Mech., **873**, pp. 72–88.

[25] Li, T., Kar, A., and Kumar, R., 2020, "Concentration Distribution of Photosensitive Liquid in a Droplet Under Ultraviolet Light," ASME J. Fluids Eng., **142**(2), p. 021301.

[26] Strasser, W., 2010, "Cyclone-Ejector Coupling and Optimisation," Prog. Comput. Fluid Dyn., **10**(1), pp. 19–31.

[27] Moffatt, H. K., 1964, "Viscous and Resistive Eddies Near a Sharp Corner," J. Fluid Mech., **18**(1), pp. 1–18.

[28] Biswas, S., and Kalita, J. C., 2018, "Moffatt Eddies in the Driven Cavity: A Quantification Study by an HOC Approach," Comput. Math. Appl., **76**(3), pp. 471–487.

[29] Masoud, H., and Felske, J. D., 2009, "Analytical Solution for Stokes Flow Inside an Evaporating Sessile Drop: Spherical and Cylindrical Cap Shapes," Phys. Fluids, **21**(4), p. 042102.

[30] Happel, J., and Brenner, H., 2012, *Low Reynolds Number Hydrodynamics: With Special Applications to Particulate Media*, Vol. 1, Springer Science & Business Media, Dordrecht, The Netherlands.